



# A 6.4yr optical quasi-periodic oscillations in SDSS J075217.84+193542.2: a new candidate for central binary black hole system

XueGuang Zhang<sup>1</sup>  

<sup>1</sup>*School of Physics and technology, Nanjing Normal University, No. 1, Wenyuan Road, Nanjing, 210023, P. R. China*

25 February 2022

## ABSTRACT

In this manuscript, a 6.4yr optical quasi-periodic oscillations (QPOs) is detected in the quasar SDSS J075217.84+193542.2 (=SDSS J0752) at a redshift 0.117, of which 13.6yr-long light curve from CSS and ASAS-SN directly described by a sinusoidal function with a periodicity 6.4yr. The 6.4yr QPOs can be further confirmed through the Generalized Lomb-Scargle periodogram with confidence level higher than 99.99%, and through the auto-correlation analysis results, and through the WWZ technique. The optical QPOs strongly indicate a central binary black hole (BBH) system in SDSS J0752. The determined two broad Gaussian components in the broad H $\alpha$  can lead to the BBH system with expected space separation about 0.02pc between the expected two central BHs with determined virial BH masses about  $8.8 \times 10^7 M_{\odot}$  and  $1.04 \times 10^9 M_{\odot}$ . Meanwhile, we check the disk precessions applied to explain the optical QPOs. However, under the disk precession assumption, the determined optical emission regions from central BH have sizes about  $40R_G$  two times smaller than sizes of the expected NUV emission regions through the correlation between disk size and BH mass, indicating the disk precessions are not preferred. And due to the lower radio loudness around 0.28, jet precessions can be also totally ruled out. Furthermore, only 0.08% probability can determined as the QPOs mis-detected through light curves randomly created by the CAR process, re-confirming the reported optical QPOs.

**Key words:** galaxies:active - galaxies:nuclei - quasars:emission lines - galaxies:Seyfert

## 1 INTRODUCTION

Optical Quasi-Periodic Oscillations (QPOs) with long periodicities of years to more than ten years have been reported in active galaxies, due to jet emissions/precessions in blazars as discussed in Sandrinelli et al. (2018); Bhatta (2019); Otero-Santos et al. (2020) or due to binary supermassive BH (BBH) systems as discussed in (Eracleous & Halpern 1994; Kormendy et al. 2009; Gaskell 2010; Barth 2015; Songshen et al. 2020). Not similar as transient QPOs arising from general relativistic effects (relativistic Frame Dragging method (Cui, Zhang & Chen 1998), discoseismology method (Wagoner 2012), etc.) related to central accreting processes in black hole X-ray binaries as discussed in van der Klis (1989, 2000); Abramowicz et al. (2004); Remillard & McClintock (2006); James et al. (2010); van den Eijnden et al. (2017); Ingram & Motta (2020) and in several Active Galactic Nuclei (AGN) as discussed in Papadakis & Lawrence (1993); McHardy et al. (2006); Gierlinski et al. (2008); Lin et al. (2013); Pasham, Strohmayr & Mushotzky (2014); Reines et al. (2016); Dorn-Wallenstein et al. (2017); Barth & Stern (2018); Smith et al. (2018); Gupta et al. (2018); Jin et al. (2021); Zhang (2021a), the QPOs related to BBH systems are due to orbital motions of two BH accreting systems leading to stronger QPOs signals which can be directly detected in the long-term light curves. In the manuscript, unless otherwise stated, the following discussed optical QPOs are the optical QPOs related to BBH systems.

Evolution from dual galactic core systems on scale of dozens to hundreds parsecs to BBH systems on scale of sub-parsecs have been accepted to be common, as the key role of galaxy mergers in evolution histories of galaxies (Begelman et al. 1980; Silk & Rees 1998; Merritt 2006; Mayer et al. 2010; Mayer 2013; Mayer & Bonoli 2019). And different techniques have been applied to detect dual core systems with the two black holes getting closer due to dynamical friction and/or BBH systems with two black holes getting closer due to emission of gravitational waves, such as based on double-peaked features of broad and/or narrow emission lines as discussed in Zhou et al. (2004); Komossa et al. (2008); Boroson & Lauer (2009); Smith et al. (2009); Shen & Loeb (2010); Eracleous et al. (2012); Popovic (2012); Comerford et al. (2013); Liu et al. (2016); Wang et al. (2017); De Rosa et al. (2019) and on spatially resolved image properties of central regions of galaxies as discussed in Komossa et al. (2003); Rodriguez et al. (2009); Piconcelli et al. (2010); Nardini (2017); Kollatschny et al. (2020) and on apparent QPOs signals detected in the long-term variability properties which are mainly considered in the manuscript.

PG 1302-102 is the well-known quasar with apparent periodic variabilities with a periodicity 1800days reported in Graham et al. (2015a), providing strong evidence for the central BBH system in PG 1302-102. More recent results on the optical QPOs in PG 1302-102 can be found in Liu et al. (2018); Kovacevic et al. (2019). Graham et al. (2015) have searched for strong Keplerian periodic signals over a baseline of nine years and reported a sample of 111 candidates with variabilities are conservative agreement with theoretical predictions from BBH systems. Charisi et al. (2016) have

\* Contact e-mail: [xgzhang@nju.edu.cn](mailto:xgzhang@nju.edu.cn)

conducted a statistical search for periodic variabilities in a sample of 35383 spectroscopically confirmed quasars, and identified 50 quasars with significant QPOs with periodicities of a few hundred days. [Liu et al. \(2015\)](#) have detected strong QPOs with a periodicity about 540days in the quasar PSO J334.2028+01.4075, leading to a reliable candidate for the central BBH system. And [Zheng \(2016\)](#) have shown the clear QPOs with a periodicity about 1500days in the quasar SDSS J0159+0105, supporting a reliable BBH system. More recently, [Serafinelli et al. \(2020\)](#) have detected the apparent QPOs with a periodicity about 1150days in the Seyfert1.5 Mrk 915, providing robust clues on the central BBH system. [Kovacevic et al. \(2020\)](#) have reported the clear QPOs with periodicity about 1.2yr in the Mrk 231 related to the central BBH system. [Liao et al. \(2021\)](#) have reported a QPOs with periodicity about 1607days with confidence level higher than 99.95% in the quasar SDSS J025214.67-002813.7 to support a central BBH system.

The reported candidates of BBH systems should produce expected background gravitational wave signals at nano-Hz frequencies, probed by the Pulsar Timing Arrays ([Foster & Backer 1990](#); [Desvignes et al. 2016](#); [Reardon et al. 2016](#); [Arzoumanian et al. 2015](#); [Verbiest et al. 2016](#)). However, for the candidates of BBH systems in [Graham et al. \(2015\)](#); [Charisi et al. \(2016\)](#), [Sesana et al. \(2018\)](#) have shown that the null hypothesis (whereby the candidates of BBH systems are false positives) is preferred over the binary hypothesis at about  $2.3\sigma$  and  $3.6\sigma$  for the candidates in [Graham et al. \(2015\)](#) and in [Charisi et al. \(2016\)](#) respectively, indicating the current candidates of BBH systems have some false candidates due to false QPOs detections. Therefore, to detect and report more candidates of BBH systems is necessary and meaningful. And in the manuscript, a new candidate of BBH system is reported.

Optical QPOs related to BBH systems, not similar as weak transient QPOs, are commonly strong enough that the QPOs can be directly detected from the long-term light curves of AGN, even considering intrinsic AGN variabilities as fundamental characteristics of AGN ([Rees 1984](#); [Ulrich et al. 1997](#); [Madejski & Sikora 2016](#); [Baldassare et al. 2020](#)) which have been proved to well described by the well-applied Continuous AutoRegressive process (CAR process or the improved damped random walk process (DRW process)) ([Kelly, Bechtold & Siemiginowska 2009](#); [Kozlowski et al. 2010](#); [Zu et al. 2013](#); [Kelly et al. 2014](#); [Starkey et al. 2016](#); [Zu et al. 2016](#); [Zhang & Feng 2017](#)). In this manuscript, a new BBH candidate is reported in the blue quasar SDSS J075217.84+193542.2 (=SDSS J0752) at a redshift 0.117 ([Paris et al. 2018](#)), due to detected optical QPOs through the long-term variabilities from the Catalina Sky Survey (CSS) ([Drake et al. 2009](#)) and from the All-Sky Automated Survey for Supernovae (ASAS-SN) ([Shappee et al. 2014](#); [Kochanek et al. 2017](#)). The shown time duration of the SDSS J0752 is two times longer than the detected periodicity, indicating the optical QPOs in SDSS J0752 should be robust to some extent. Moreover, the time duration from 2005 to 2013 in CSS of the SDSS J0752 is only about a little more than one cycle (considering the following determined 6.4year periodicity), leading the SDSS J0752 not included in the sample of candidates of BBH systems in [Graham et al. \(2015\)](#) with observing time durations in CSS larger than 1.5 cycles.

The manuscript is organized as follows. Section 2 presents main results on the long-term optical variabilities of SDSS J0752. Section 3 shows main results on the spectroscopic properties of SDSS J0752. Section 4 gives the necessary discussions on the probable central BBH system. Section 5 gives final summaries and conclusions. Here, the cosmological parameters have been adopted as  $H_0 = 70 \text{ km} \cdot \text{s}^{-1} \text{ Mpc}^{-1}$ ,  $\Omega_\Lambda = 0.7$  and  $\Omega_m = 0.3$ .

## 2 LONG-TERM OPTICAL VARIABILITIES IN SDSS J0752

### 2.1 Optical QPOs in SDSS J0752

The CSS V-band light curve is collected from <http://nesssi.cacr.caltech.edu/DataRelease/> with MJD-2453000 from 469 (April 2005) to 3596 (October 2013), and the ASAS-SN V-band light curve is collected from <https://asas-sn.osu.edu/> with MJD-2453000 from 2974 (February 2012) to 5452 (November 2018). Left panel of Figure 1 shows the long-term photometric V-band light curve. Here, we do not show the ASAS-SN g-band data points in Figure 1, because of the unknown magnitude difference between ASAS-SN V-band and ASAS-SN g-band and of the short time duration of the ASAS-SN g-band light curve. And moreover, similar as what have been done to the light curves from the CSS and from the ASAS-SN in the PG 1302-102 discussed in [Liu et al. \(2018\)](#), the magnitude difference 0.2019 is accepted, based on the data points in time duration with MJD-2453000 from 2973 to 3597 covered both in the CSS and in the ASAS-SN.

Then, by both Levenberg-Marquardt least-squares minimization technique and Maximum Likelihood Method combining with Markov Chain Monte Carlo (MCMC) technique ([Foreman-Mackey et al. 2013](#)), a simple sinusoidal function plus a linear trend are applied to determine the best descriptions to the 13.6yr-long light curve, with  $\chi^2/Dof \sim 1.28$  ( $\chi^2$  and Dof as the summed squared residuals and the degree of freedom). Here, the main objective of applications of sinusoidal function is to show clearer clues on optical QPOs. The best-fitting results are shown in left panel of Figure 1 by a linear trend plus a sinusoidal function

$$LMC = A + B \times \frac{t}{1000\text{days}} + C \times \sin\left(\frac{2\pi t}{T_{QPOs}} + \phi_0\right) \quad (1)$$

with  $A = 15.223 \pm 0.012$ ,  $B = 0.103 \pm 0.003$ ,  $C = 0.119 \pm 0.007$ ,  $T_{QPOs} = 2321 \pm 32$ ,  $\phi_0 = 1.159 \pm 0.131$ , leading to the QPOs with a periodicity of  $2321 \pm 32$  days. Moreover, based on the F-test technique, the corresponding 99.9999% confidence bands to the best fitting results are shown in left panel of Figure 1. Then, based on the determined periodicity, the phase folded light curve  $LMC_{pf}$  shown in the right panel of Figure 1 can also be well described by a sinusoidal function plus a linear trend

$$LMC_{pf} = A + B \times \frac{t}{1000\text{days}} + C \times \sin(2\pi t + \phi_0) \quad (2)$$

with  $A = 15.475 \pm 0.013$ ,  $B = 0.152 \pm 0.026$ ,  $C = -0.142 \pm 0.008$ ,  $\phi_0 = -0.753 \pm 0.061$ . And based on the F-test technique, the corresponding 99.9999% confidence bands to the best fitting results are also shown in right panel of Figure 1. The directly fitted results by the sinusoidal function to both the light curve and the phase folded light curve strongly support the optical QPOs in SDSS J0752.

Besides the direct fitting results shown in Figure 1 by the sinusoidal function, the improved Generalized Lomb-Scargle (GLS) periodogram ([Lomb 1976](#); [Scargle 1982](#); [Zechmeister & Kurster 2009](#); [VanderPlas 2018](#)) is applied to check the periodicities in the long-term variabilities in SDSS J0752, similar as what have been discussed in [Zheng \(2016\)](#). Higher than 99.99% confidence level determined by the bootstrap method as discussed in ([Ivezic et al. 2019](#)), there are two periodicities around 350days and 2400days detected by the GLS periodogram shown in the left panel of Figure 2. The GLS-determined periodicity about 2400days is well consistent with the determined 2321days shown in Figure 1. Further discussions are shown on the GLS-determined periodicity around 350days by the following two points. First, accepted the periodicity around 350days,

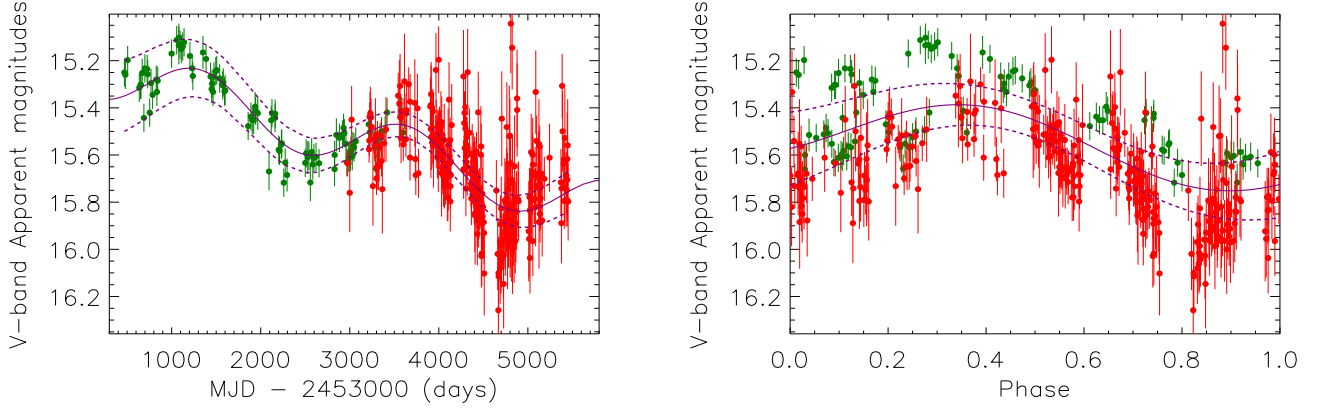


**Figure 1.** Left panel shows the long-term light curve from the CSS (in dark green) and from the ASAS-SN (in red color). Right panel shows the corresponding phase folded light curve based on the determined periodicity of 2321 days. In each panel, solid and dashed lines in purple show the best descriptions to the whole light curve and the corresponding 99.9999% confidence bands, based on a sinusoidal function plus a linear trend.

properties of the phase-folded light curve is re-checked. However, there are no sine-like variabilities in the phase-folded light curve with the periodicity around 350days. Second, the auto-correlation analysis (ACF) is applied to check the periodicities, shown in the right panel of Figure 2. It is clear that only the time-lag around 2300days can lead to a clear peak in the cross correlation results, and no maximum peaks can be well detected around 350days in the ACF results. Moreover, QPOs in SDSS J0752 is also determined through the commonly applied weighted wavelet z-transformation (WWZ) technique (Foster 1996) which have been well applied to determine QPOs as more recently discussed in An et al. (2016); Gupta et al. (2018); Kushwaha et al. (2020); Li et al. (2021). The power maps determined by the WWZ technique are shown in Fig. 3 in SDSS J0752, leading to a clear peak around 2310days but no clear peaks around 300days. Therefore, the periodicity around 2300days is well accepted, and the periodicity around 350days is not considered any more in the manuscript.

Furthermore, the commonly accepted bootstrap method (VanderPlas 2018) is applied to test robustness of the GLS-determined periodicity around 2400days in SDSS J0752. Among the shown data points in left panel of Figure 1, about half of the data points are randomly collected to create a new light curve. Then, the GLS periodogram is applied to the new light curve to test whether the expected periodicity around 2400days has significance level lower than 99.99%. Among 1000000 created light curves by randomly collected data points, there is no one new light curve has its GLS-determined periodicity with significance level lower than 99.99%. Therefore, the false positive rate is less than  $10^{-6}$  for the GLS-determined periodicity in left panel of Figure 2 in SDSS J0752.

Finally, the QPOs with a periodicity around 2320days in SDSS J0752 can be well detected from the long-term light curve (time duration about 2.1 times longer than the detected periodicity) with confidence level higher than 99.99%, based on the best-fitting results directly by the sinusoidal function shown in the left panel of Figure 1, on the sine-like phase-folded light curve shown in the right panel of Figure 1, on the results of GLS periodogram shown in the left panel of Figure 2, on the ACF results shown in the right panel of Figure 2 and on the power maps determined by the WWZ technique shown in Figure 3.

## 2.2 Mis-detected QPOs in long-term AGN variabilities?

As more recently discussed in Vaughan et al. (2016), false periodicities can be expected in quasar time-domain surveys. Therefore, it is necessary and interesting to determine whether the determined optical QPOs was mis-detected QPOs in the long-term optical variabilities of SDSS J0752, although the different techniques applied in the subsection above can lead to the detected optical periodicity in SDSS J0752. In the subsection, similar as the considered statistical method in Markowitz, Reeves & Braitto (2016) to assess the significance of an absorption line in X-ray spectra, the following procedure is applied to estimate the probability to detected mis-detected QPOs in light curves well described by random walk process.

It is well known that the CAR (or DRW) process is preferred to describe the intrinsic long-term AGN variabilities. Here, the DRW process is also applied to describe the long-term variabilities of SDSS J0752, through the public code JAVELIN (Just Another Vehicle for Estimating Lags In Nuclei) (Kozłowski et al. 2010; Zu et al. 2013) with two well accepted parameters of intrinsic characteristic variability amplitude and timescale of  $\sigma$  and  $\tau$ . The best descriptions to the light curve are shown in the left panel of Figure 4. And the corresponding MCMC determined two dimensional posterior distributions of the parameters of  $\sigma$  and  $\tau$  are shown in the right panel of Figure 4, with the determined  $\ln(\tau/\text{days}) \sim 7.23 \pm 0.57$  ( $\tau \sim 1385$ days) and  $\ln(\sigma/(\text{mag}/\text{days}^{1/2})) \sim -1.64 \pm 0.27$  ( $\sigma \sim 0.19\text{mag}/\text{day}^{1/2}$ ). Comparing with the long-term variabilities of SDSS quasars shown in Figure 3 in MacLeod et al. (2010), the DRW determined  $\tau \sim 1385$ days is apparently one magnitude longer than the mean value around 200days of the SDSS quasars, and the DRW determined  $\log(SF_\infty/\text{mag}) = \log(\sigma \times \sqrt{\tau}) \sim 0.86$  is definitely one magnitude larger than the mean value around -0.7 of the SDSS quasars. The larger values of  $\sigma$  and  $\tau$  than the common values of the SDSS quasars indicate SDSS J0752 is an interesting target.

Based on the CAR process discussed in Kelly, Bechtold & Siemiginowska (2009):

$$dLMC_t = \frac{-1}{\tau} LMC_t dt + \sigma \sqrt{dt} \epsilon(t) + 15.62 \quad (3)$$

where  $\epsilon(t)$  a white noise process with zero mean and variance equal to 1, it is interesting to check whether CAR process determined long-term variability can lead to mis-detected QPOs. Here, the mean

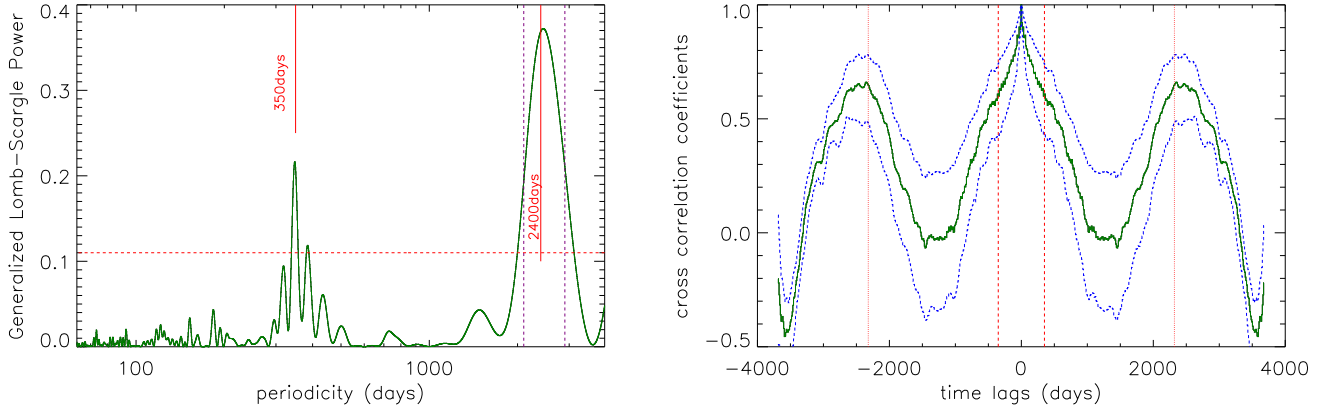


**Figure 2.** Left panel shows results through the Generalized Lomb-Scargle periodogram. In the left panel, horizontal dashed red line shows the 99.99% confidence level through the bootstrap method. The vertical red lines mark the two peaks around 350days and around 2400days. The vertical dashed purple lines (at 2100days and at 2900days) mark the periodicity width at the half maximum for the periodicity around 2400days. Right panel shows the ACF results. In the right panel, solid dark green line and dashed blue lines show the ACF results and the corresponding uncertainties determined by the bootstrap method. The vertical dashed and dotted red lines mark the positions with time lags at  $\pm 350$ days and at  $\pm 2320$ days, respectively.

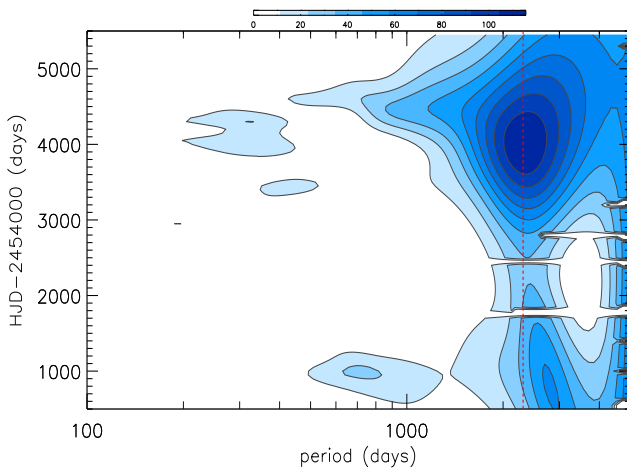


**Figure 3.** The power maps in SDSS J0752 determined by the WWZ technique with frequency step of 0.00001 and searching periods from 100days to 5000days applied to the light curve shown in left panel of Figure 1. The vertical red dashed line marks the position with periodicity about 2310days.

value of  $LMC_t$  is set to be 15.62 (the mean value of the observational light curve of SDSS J0752), which has no effects on the following results. Then, a series of 10000 simulating light curves  $[t_i, LMC_i]$  are created, with randomly selected values of  $\tau$  from 50days to 1000days and the  $\sigma_*$  (the parameter in unit of mag in the CAR process in Kelly, Bechtold & Siemiginowska (2009) slightly different from the  $\sigma$  applied in the JAVELIN) leading the variance  $\tau\sigma_*^2/2$  to be 0.047 (the variance of the observational light curve of SDSS J0752), and  $t_i$  are the same as the observational time information shown in Figure 1. And the similar uncertainties  $LMC_{t, err}$  are simply added to the simulating light curves  $LMC_t$  by

$$LMC_{t, err} = LMC_t \times \frac{L_{err}}{L_{obs}} \quad (4)$$

with  $L_{obs}$  and  $L_{err}$  as the observational light curve and the corresponding uncertainties shown in left panel of Figure 1.

Then, the following two criteria are applied to check whether QPOs can be detected in the simulating light curves. First, GLS-determined periodicities should be around 2300days (larger than 2100days and smaller than 2900days, estimated from the corresponding periodicity width at the half maximum marked by vertical dashed purple lines in left panel of Figure 2) with significance level higher than 99.99%. Second, periodicities determined by the ACF results should be around 2300days (larger than 2100days and smaller than 2900days) with cross correlation coefficients higher than 0.5. Finally, among the 10000 simulating light curves, there are 8 light curves with expected mis-detected QPOs, accepted the two criteria above. Moreover, Figure 5 shows 2 of the 8 simulating light curves with mis-detected QPOs and the corresponding best-fitting results by the sinusoidal function. The results indicate that the DRW process (or the CAR process) can lead to light curves with mathematical determined QPOs (the mis-detected QPOs, or the fake QPOs), however, the probability of the mis-detected QPOs in CAR-process simulating light curves is around 0.08% (8/10000). The results strongly indicate that the probability higher than 99.92% (1-0.08%) to support that the detected optical QPOs in SDSS J0752 are not mis-detected QPOs from a pure DRW process described light curve.

### 3 SPECTROSCOPIC PROPERTIES OF SDSS J0752

Figure 6 shows the high-quality galactic reddening corrected ( $E(B-V) = 0.0448$ ) spectrum of SDSS J0752 with PLATE-MJD-FIBERID=1582-52939-0612. The apparently blue continuum emissions lead SDSS J0752 to be well classified as a SDSS quasar. The featureless continuum emissions can be well described by a power law function,  $f_\lambda \propto \lambda^{-0.51}$  through the following four windows [4150Å, 4250Å], [4528Å, 4614Å], [5462Å, 5873Å] and [7553Å, 8200Å], leading the continuum luminosity at rest wavelength 5100Å to be about  $\lambda L_{5100} = 2.12 \times 10^{44}$  erg/s.

Then, emission lines around  $H\alpha$  in SDSS J0752 can be well measured, similar as what we have recently done in Zhang (2021b,c). Left



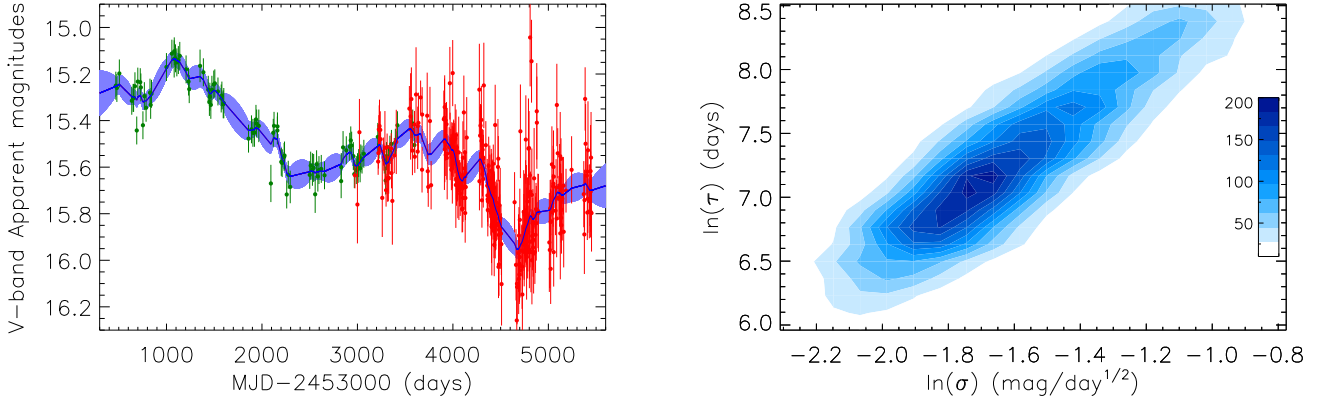


**Figure 4.** Left panel shows the DRW-determined best descriptions to the long-term variabilities of SDSS J0752. Solid blue line and area filled with light blue show the best descriptions and the corresponding  $1\sigma$  confidence bands. Symbols in dark green and in red represent the data values from the CSS and from the ASAS-SN. Right panel shows the MCMC determined two-dimensional posterior distributions of the DRW model parameters of  $\ln(\tau)$  and  $\ln(\sigma)$ .

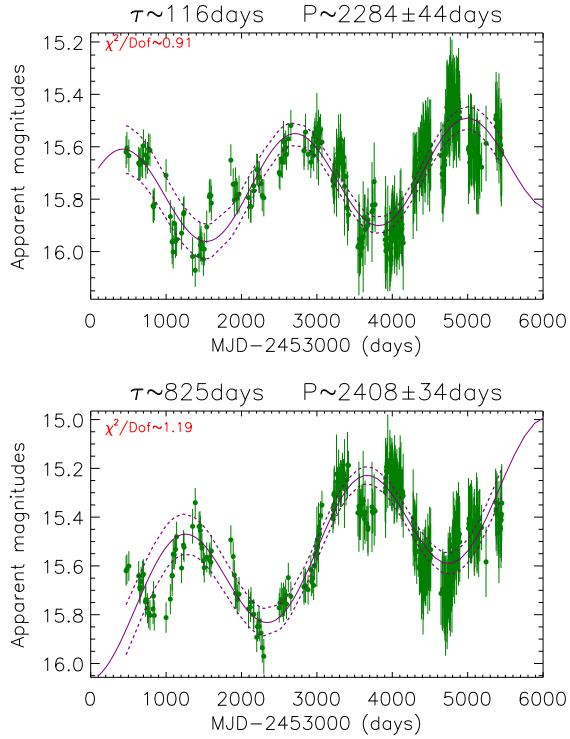


**Figure 5.** Two examples on probable mis-detected QPOs in the simulating light curves by the CAR process. In each panel, solid dark green circles plus error bars show the simulating light curve, solid and dashed lines in purple show the best descriptions to the light curve and the corresponding 99.9999% confidence bands, based on the sinusoidal function plus a linear trend. The input value of  $\tau$  and the calculated periodicity  $P$  are marked in the title of each panel. And the calculated  $\chi^2/Dof$  is marked in the top left corner in each panel.

panel of Figure 7 shows the emission lines within rest wavelength range from 6200Å to 6850Å, including [O I]λ6300, 6363Å doublet, [N II]λ6548, 6583Å doublet, broad and narrow Hα, and [S II]λ6716, 6731Å doublet. The following model functions are

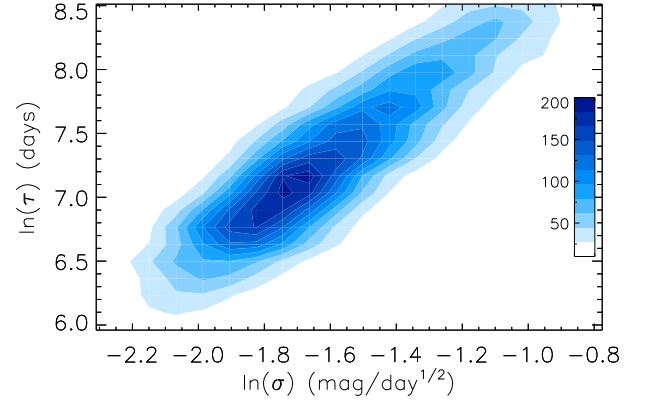


**Figure 6.** The galactic reddening corrected spectrum of SDSS J0752 in rest frame. The dotted red line represents the determined power-law continuum emissions. The areas filled with green lines show the wavelength windows applied to determine the power law continuum emissions.

applied to describe the emission lines, in order to obtain further clear properties of the broad components in the Hα. There are two broad Gaussian functions applied to describe the broad Hα, two Gaussian functions applied to describe each narrow emission line (a core component plus an extended component, similar as discussed in [O III] doublet in Greene & Ho (2005a); Shen et al. (2011); Zhang (2021b)), and a power law function applied to describe the AGN continuum emissions underneath the emission lines. Through the Levenberg-Marquardt least-squares minimization technique, the emission lines around Hα can be well fitted. When the fitting procedure is running, only two restrictions are accepted. On the one hand, the flux ratios of components in [N II] doublet are set to the theoretical values of 3. On the other hand, the emission flux of each Gaussian emission component is not smaller than zero. The best-fitting results  $Y_{fit}$  and the corresponding residuals  $(Y - Y_{fit})/Y_{err}$  (where  $Y$  and  $Y_{err}$  represents the SDSS spectrum and the corresponding uncertainties) are shown in Figure 7, with  $\chi^2/dof \sim 0.64$ . The measured line parameters are listed in Table 1.

Moreover, in order to confirm the extended components in narrow emission lines around Hα and the two broad Gaussian components in broad Hα, the other one model is considered by including

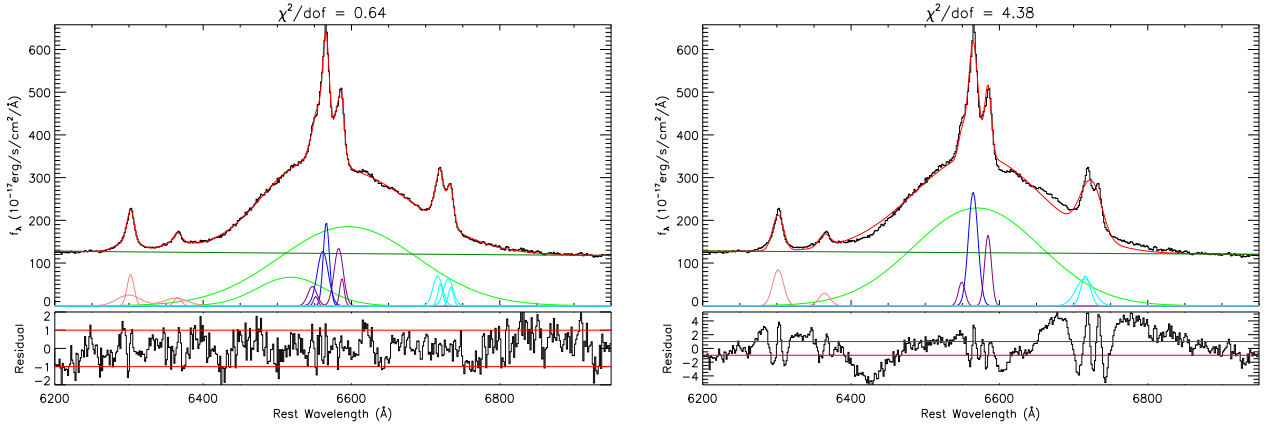


**Figure 7.** Left panel shows the best-fitting results (top region) and the corresponding residuals (bottom region) to the emission lines around the  $H\alpha$ , by two broad Gaussian components in broad  $H\alpha$ , a core and an extended components in each narrow emissions line. In top region, solid black line shows the observed SDSS spectrum, solid red line shows the best-fitting results, solid dark green line shows the determined power law continuum emissions, solid green lines show the determined two broad components in the broad  $H\alpha$ , solid blue lines show the determine core and extended components in the narrow  $H\alpha$ , solid pink lines show the determined core and extended components in the  $[O\text{ I}]$  doublet, solid purple lines show the determine core and extended components in the  $[N\text{ II}]$  doublet, and solid cyan lines show the determined core and extended components in the  $[S\text{ II}]$  doublet. In the bottom region, solid red lines show  $Residual = \pm 1$ . Right panel shows the best-fitting results (top region) and the corresponding residuals (bottom region) to the emission lines around the  $H\alpha$ , by one broad Gaussian component in broad  $H\alpha$ , one Gaussian component in each narrow emissions line. In top region, solid black line shows the observed SDSS spectrum, solid red line shows the best-fitting results, solid dark green line shows the determined power law continuum emissions, solid green line shows the determined broad component in  $H\alpha$ , solid blue line shows the determined narrow component in  $H\alpha$ , solid purple lines show the determined  $[N\text{ II}]$  doublet, solid cyan lines show the determined  $[S\text{ II}]$  doublet, and solid pink lines show the determined  $[O\text{ I}]$  doublet. In the bottom region, solid red lines show  $Residual = \pm 1$ .

**Table 1.** Line parameters

line		$\lambda_0$	$\sigma$	flux
Broad $H\alpha$		$6517.7 \pm 2.4$	$45.1 \pm 2.6$	$73 \pm 9$
		$6594.9 \pm 1.6$	$93.8 \pm 0.6$	$440 \pm 8$
Broad $H\beta$		$4827.9 \pm 1.9$	$33.4 \pm 2.1$	$14 \pm 2$
		$4885.1 \pm 1.1$	$69.5 \pm 0.4$	$82 \pm 3$
$[O\text{ III}]\lambda 5007\text{\AA}$	c	$5008.4 \pm 0.1$	$3.9 \pm 0.1$	$84 \pm 2$
	e	$5004.2 \pm 0.1$	$11.6 \pm 0.2$	$59 \pm 2$
Narrow $H\beta$	c	$4863.6 \pm 0.3$	$3.0 \pm 0.3$	$5.1 \pm 1.2$
	e	$4859.7 \pm 1.2$	$6.2 \pm 0.6$	$5.6 \pm 1.3$
Narrow $H\alpha$	c	$6566.2 \pm 0.3$	$3.9 \pm 0.2$	$18 \pm 2$
	e	$6561.4 \pm 0.2$	$7.2 \pm 0.4$	$25 \pm 2$
$[N\text{ II}]\lambda 6583\text{\AA}$	c	$6586.8 \pm 0.2$	$3.4 \pm 0.4$	$6.7 \pm 1.3$
	e	$6582.1 \pm 0.2$	$6.4 \pm 0.5$	$19.5 \pm 1.5$
$[O\text{ I}]\lambda 6300\text{\AA}$	c	$6302.2 \pm 0.2$	$4.7 \pm 0.2$	$8.7 \pm 0.4$
	e	$6299.5 \pm 0.7$	$16.8 \pm 1.1$	$10.7 \pm 0.6$
$[O\text{ I}]\lambda 6363\text{\AA}$	c	$6365.7 \pm 0.2$	$4.8 \pm 0.2$	$2.4 \pm 0.2$
	e	$6362.9 \pm 0.6$	$16.9 \pm 1.1$	$7.6 \pm 0.6$
$[S\text{ II}]\lambda 6716\text{\AA}$	c	$6719.6 \pm 0.3$	$3.3 \pm 0.5$	$4.2 \pm 1.7$
	e	$6716.2 \pm 0.7$	$6.4 \pm 0.4$	$11.1 \pm 1.9$
$[S\text{ II}]\lambda 6731\text{\AA}$	c	$6734.1 \pm 0.3$	$3.4 \pm 0.5$	$3.7 \pm 1.5$
	e	$6730.6 \pm 0.6$	$6.4 \pm 0.4$	$10.2 \pm 1.5$

Notice: The first column shows which line is measured. The second column shows which component is determined in the narrow emission lines, 'c' means the core component, 'e' means the extended component. The third, fourth and fifth columns show the measured line parameters: the center wavelength  $\lambda_0$  in unit of  $\text{\AA}$ , the line width (second moment)  $\sigma$  in unit of  $\text{\AA}$  and the line flux in unit of  $10^{-15} \text{ erg/s/cm}^2$ .

For the broad  $H\alpha$  and broad  $H\beta$ , there are two Gaussian components.

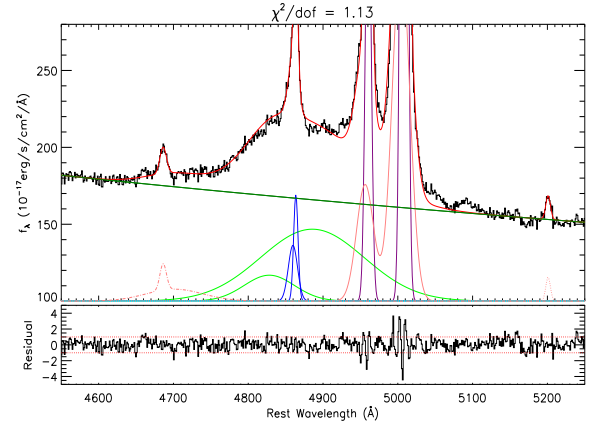


**Figure 8.** Best-fitting results (top region) and the corresponding residuals (bottom region) to the emission lines around the  $H\beta$ . In top region, solid black line shows the observed SDSS spectrum around  $H\beta$ , solid red line shows the best-fitting results, solid dark green line shows the determined power law continuum emissions, solid green lines show the determined two broad components in the broad  $H\beta$ , solid blue lines show the determine core and extended components in the narrow  $H\beta$ , solid lines in purple and in pink show the determine core and extended components in the  $[O\text{ III}]\lambda 5007\text{\AA}$  doublet, dot-dashed pink line shows the determined broad and narrow component of  $\text{He II}$  line, and dotted pink line shows the determined  $[N\text{ I}]\lambda 5205\text{\AA}$  line. Here, in top region, the plots are shown with  $f_\lambda$  smaller than  $200 \times 10^{-17} \text{ erg/s/cm}^2/\text{textsc}$ , in order to clearly show the broad components in the  $H\beta$ . In the bottom region, solid red lines show  $Residual = \pm 1$ .

the following model functions. There is only one broad Gaussian function applied to describe the broad  $H\alpha$ , one Gaussian function applied to describe each narrow emission line. Then, through the same Levenberg-Marquardt least-squares minimization technique, the best fitting results and corresponding residuals are shown in the right panel of Figure 7 with  $\chi^2/dof \sim 4.38$ . Therefore, it is neces-

sary and reasonable to consider the two broad Gaussian components in  $H\alpha$  and the extended components in the narrow emission lines.

Meanwhile, Figure 8 shows the best fitting results (with  $\chi^2/dof \sim 1.13$ ) to the emission lines around  $H\beta$  with rest wavelength from 4450Å to 5350Å by the following model functions through the same Levenberg-Marquardt least-squares minimization technique, to support the similar line profiles between broad  $H\alpha$  and broad  $H\beta$ . There are two broad Gaussian components applied to describe the broad  $H\beta$ , four Gaussian components applied to describe the core and extended components in [O III] doublet, two Gaussian components applied to describe the core and the extended component in narrow  $H\beta$ , one Gaussian component applied to describe the narrow [N I] $\lambda$ 5205Å, two Gaussian functions applied to describe the broad and narrow He I, and a power law component applied to describe the continuum emissions underneath the emission lines. When the fitting procedure is running, the redshift and the line width of the two broad components in the broad  $H\beta$  are the same as those of the two broad components in the broad  $H\alpha$ , and the flux ratios of the components of the [O III] doublet are set to the theoretical values of 3. The measured line parameters of the emission lines around  $H\beta$  are also listed in Table 1.

It is clear that the broad  $H\alpha$  includes two broad components with line parameters of  $[\lambda_0, \sigma_l, f]$  (rest central wavelength in unit of Å, second moment in unit of Å and line flux in unit of  $10^{-15}$  erg/s/cm<sup>2</sup>) as [6517.7±2.4, 45.1±2.6, 73±9] and [6594.9±1.6, 93.8±0.6, 440±8]. In order to confirm the two broad components, new model functions with only one broad Gaussian component to describe the broad  $H\alpha$  but two components (core and extended) to describe each narrow emission line are applied to re-describe the emission lines around the  $H\alpha$ , leading to  $\chi^2/dof \sim 3.03$ , strongly indicating that the two broad components are preferred in the broad  $H\alpha$ : one blue-shifted component with shifted velocity about  $2168 \pm 110$  km/s and one red-shifted component with shifted velocity about  $1384 \pm 74$  km/s, based on the central wavelength difference between the broad component and the core component of the narrow  $H\alpha$  with line parameters listed in Table 1. Here, the best fitting results and corresponding residuals are not shown for the model functions with one broad Gaussian component applied to describe the broad  $H\alpha$  and two components applied to describe each narrow emission line, due to similar residuals with rest wavelength from 6400Å to 6800Å shown in the right panel of Figure 7.

#### 4 MAIN DISCUSSIONS

The determined two broad  $H\alpha$  components provide better chances to check whether is there a central BBH system in SDSS J0752, because the two BH masses in the probable BBH system can be well determined by properties of the two broad components. Accepted assumption of a central BBH system in SDSS J0752, through the virialization assumption (Peterson et al. 2004; Vestergaard & Peterson 2006) to broad line emission clouds combining with the empirical R-L relation Bentz et al. (2013) to determine the distance between emission clouds and central BH, the virial BH mass can be estimated through the formula discussed in Greene & Ho (2005)

$$\frac{M_{BH}}{M_{\odot}} = 2.2 \times 10^6 \times \left( \frac{L_{H\alpha}}{10^{42} \text{erg/s}} \right)^{0.56} \times \left( \frac{FWHM_{H\alpha}}{1000 \text{km/s}} \right)^{2.06} \quad (5)$$

. Here, the more recent R-L relation discussed in Bentz et al. (2013) is applied. Then, based on the line luminosities and line widths of the two broad Gaussian components, the two BH masses can be estimated as  $M_{BH,b} = (8.8 \pm 1.7) \times 10^7 M_{\odot}$  for the blue-shifted BH

system and  $M_{BH,r} = (104.4 \pm 3.1) \times 10^7 M_{\odot}$  for the red-shifted BH system. Then, following the discussed results in Eracleous et al. (2012), the space separation between the central two BHs can be estimated as

$$A_{BBH} = 0.432 \times M_8 \times \left( \frac{P_{BBH}/\text{year}}{2652 M_8} \right)^{2/3} \sim 0.02 pc \quad (6)$$

where  $M_8$  represent the total BH mass of the BBH system in unit of  $10^8 M_{\odot}$  and  $P_{BBH} \sim 6.4$ yr represents the orbital period of the BBH system.

Meanwhile, besides the BBH system, precessions of emission regions with probable hot spots for the optical continuum emissions can also be applied to describe the detected optical QPOs in SDSS J0752. Not considering two independent broad  $H\alpha$  components, line properties of the total broad  $H\alpha$  can be applied to estimate the central virial BH mass as  $1.87 \times 10^9 M_{\odot}$ , through the formula discussed in Peterson et al. (2004)

$$M_{BH} = 5.5 \times \frac{\sigma_{\text{broad},H\alpha}^2 \times R_{\text{BLRs}}}{G} \quad (7)$$

where  $\sigma_{\text{broad},H\alpha} \sim 4010$  km/s represents the second moment of the total broad  $H\alpha$  and  $R_{\text{BLRs}} \sim 54$  light-days is the distance of broad line emission regions to central BH estimated through the R-L relation (Bentz et al. 2013) with the continuum luminosity at 5100Å about  $2.12 \times 10^{44}$  erg/s shown in Figure 6. Then, as discussed in Eracleous et al. (1995) and in Storchi-Bergmann et al. (2003), the expected disk precession period can be estimated as

$$T_{\text{pre}} \sim 1040 M_8 R_3^{2.5} \text{yr} \quad (8)$$

, where  $R_3$  and  $M_8 \sim 18.7$  mean the distance of emission regions to central BH in unit of  $10^3 R_G$  ( $R_G = \frac{GM_{BH}}{c^2}$ ) and the BH mass in unit of  $10^8 M_{\odot}$ . In order to get the detected periodicity about 6.4yr, the expected  $R_3$  could be around 0.041 ( $41 R_G$ ). However, based on the discussed results on the distance of NUV emission regions to central BHs in Morgan (2010) through the microlensing variability properties of eleven gravitationally lensed quasars, the NUV 2500Å continuum emission regions in SDSS J0752 have distance from central BH as

$$\log \frac{R_{2500}}{cm} = 15.78 + 0.80 \log \left( \frac{M_{BH}}{10^9 M_{\odot}} \right) \sim (72 \pm 20) R_G \quad (9)$$

The estimated NUV emission regions have distances about two times larger than the optical continuum emission regions in SDSS J0752 under the disk precession assumption. The unreasonable results strongly indicate that the disk precessions of emission regions are not preferred to be applied to explain the detected optical QPOs in SDSS J0752.

Moreover, an oscillating recoiled supermassive black hole (rSMBH) scenario has been well discussed in Kim et al. (2018), and the rSMBH scenario has been applied to explain the observed velocity offsets of the blue/red-shifted components in asymmetric broad emission lines in Mrk1018. Therefore, it is interesting to consider whether the rSMBH scenario can be applied to explain the blue/red-shifted components in broad Balmer lines in SDSS J0752. As discussed in Kim et al. (2018), the rSMBH scenario can lead to constant velocity offset difference between blue-shifted and red-shifted broad components, however, BBHs system should lead to time dependent velocity offset difference between blue-shifted and red-shifted broad components. However, due to single-epoch spectra of SDSS J0752, properties of velocity offset difference can not be applied to determine whether the rSMBH scenario is preferred or

not. However, [Kim et al. \(2018\)](#) also discussed that a BBH system can indicate that a broad emission component with larger velocity offset will have a smaller line width at each epoch. In broad Balmer lines of SDSS J0752, the blue-shifted component has velocity offset  $47\text{\AA}$  and line width  $45.1\text{\AA}$ , but the red-shifted component has velocity offset  $31\text{\AA}$  and line width  $93.8\text{\AA}$ , consistent with the expected results by a BBH system: the blue-shifted component has larger velocity offset but smaller line width. Therefore, in the current stage, the BBH system is preferred in SDSS J0752, unless there are long enough spectroscopic variabilities of broad emission lines in SDSS J0752.

As discussed in Introduction, long-term QPOs can be detected in blazars due to jet precessions. However, radio power at 1.4GHz is about 25mJy in SDSS J0752, provided by the NVSS (NRAO VLA Sky Survey, [Obric et al. \(2006\)](#)). Combining with the optical luminosity at  $5100\text{\AA}$ , the radio loudness of SDSS J0752 is about  $R \sim 0.28$ , indicating SDSS J0752 is a radio quiet AGN. Therefore, jet precessions can be well ruled out to explain the optical QPOs in SDSS J0752.

## 5 SUMMARIES AND CONCLUSIONS

The main conclusions are as follows.

- The long-term light curve from the CSS and the ASAS-SN can be well described by a sinusoidal function with a periodicity about 2321 days (6.4yr) in SDSS J0752, which can be further confirmed by the corresponding sine-like phase folded light curve.
- The periodicity can be re-confirmed by the Generalized Lomb-Scargle periodogram with confidence level higher than 99.99%, and by the auto-correlation analysis results, and by the WWZ technique.
- The long-term optical QPOs can be applied as the better indicators to the central BBH system in SDSS J0752. Based on the two broad  $H\alpha$  components, the virial BH masses of the two central BHs can be estimated as  $8.8 \times 10^7 M_{\odot}$  and  $1.04 \times 10^9 M_{\odot}$ , leading the BBH system expected space separation is about 0.02pc.
- Based on the estimated sizes about  $70R_G$  of the NUV emission regions about two times larger than the disk precession expected sizes about  $41R_G$  of the optical emission regions, the disk precessions can be well ruled out to explain the detected QPOs in SDSS J0752. Meanwhile, the radio loudness about 0.28 strongly support that the jet precessions can be totally ruled out to explain the detected QPOs in SDSS J0752.
- Based on the mathematical CAR process simulating light curves as the intrinsic AGN variabilities, 0.08% probability can be determined to detect mis-detected QPOs in the simulating light curves. Therefore, the optical QPOs in SDSS J0752 are more confident.

## ACKNOWLEDGEMENTS

Zhang gratefully acknowledge the anonymous referee for giving us constructive comments and suggestions to greatly improve our paper. Zhang gratefully acknowledges the kind support of Starting Research Fund of Nanjing Normal University, and the kind grant support from NSFC-12173020. This paper has made use of the data from the SDSS projects. The SDSS-III web site is <http://www.sdss3.org/>. SDSS-III is managed by the Astrophysical Research Consortium for the Participating Institutions of the SDSS-III Collaboration. This paper has made use of the data from the CSS projects <http://nesssi.cacr.caltech.edu/DataRelease/> and the ASAS-SN projects <https://asas-sn.osu.edu/>.

## DATA AVAILABILITY

The data underlying this article will be shared on reasonable request to the corresponding author ([xgzhang@nynu.edu.cn](mailto:xgzhang@nynu.edu.cn)).

## REFERENCES

- Abramowicz, M. A., Kluzniak, W., McClintock, J. E., Remillard, R. A., 2004, *ApJL*, 609, L63
- An, T.; Lu, X.; Wang, J., 2016, *A&A*, 585, 89
- Arzoumanian, Z., Brazier, A., Burke-Spolaor, S., et al., 2015, *ApJ*, 813, 65
- Baldassare, V. F.; Geha, M.; Greene, J., 2020, *ApJ*, 896, 10
- Barth, A. J.; Stern, D., 2018, *ApJ*, 859, 10
- Barth, A. J.; Bennert, V. N.; Canalizo, G.; et al., 2015, *ApJS*, 217, 26
- Begelman, M. C., Blandford, R. D., Rees, M. J., 1980, *Natur*, 287, 307
- Bentz M. C., et al., 2013, *ApJ*, 767, 149
- Bhatta, G., 2019, *Universe Proceedings*, 17, 15, arXiv:1909.10268
- Boroson, T. A., Lauer, T. R. 2009, *Nature*, 458, 53
- Charisi, M.; Bartos, I.; Haiman, Z.; et al., 2016, *MNRAS*, 463, 2145
- Comerford, J. M., Schluns, K., Greene, J. E., Cool, R. J., 2013, *ApJ*, 777, 64
- Cui, W.; Zhang, S. N.; Chen, W., 1998, *ApJL*, 492, L53
- Desvignes, G., Caballero, R. N., Lentati, L., et al., 2016, *MNRAS*, 458, 3341
- De Rosa, A.; Vignali, C.; Bogdanovic, T., et al., 2019, *NewAR*, 86, 101525
- Dorn-Wallenstein, T.; Levesque, E. M.; Ruan, J. J., 2017, *ApJ*, 850, 86
- Drake, A. J.; Djorgovski, S. G.; Mahabal, A., et al., 2009, *ApJ*, 696, 870
- Eracleous, M.; Halpern, J. P., 1994, *ApJS*, 90, 1
- Eracleous, M.; Livio M., Halpern, J. P., 1995, *ApJ*, 438, 610
- Eracleous, M.; Boroson, T. A.; Halpern, J. P.; Liu, J., 2012, *ApJS*, 201, 23
- Foreman-Mackey, D.; Hogg, D. W.; Lang, D.; Goodman, J., 2016, *PASP*, 125, 306
- Foster, R. S., & Backer, D. C. 1990, *ApJ*, 361, 300
- Foster, G., 1996, *AJ*, 112, 1709
- Gaskell, C. M., 2010, *Natur*, 463, 1
- Gierlinski, M.; Middleton, M.; Ward, M.; Done, C., 2008, *Nature*, 455, 369
- Graham, M. J.; Djorgovski, S. G.; Stern, D., et al., 2015a, *Natur*, 518, 74
- Graham, M. J., Djorgovski, S. G., Stern, D., et al., 2015, *MNRAS*, 453, 1562
- Greene, J. E.; Ho, L. C., 2005a, *ApJ*, 627, 721
- Green, J. E., Ho, L. C., 2005, *ApJ*, 630, 122
- Gupta, A. C.; Tripathi, A.; Wiita, P. J.; et al., 2018, *A&A*, 616, 6
- Kim, D. C.; Yoon, I.; Evans, A. S., 2018, *ApJ*, 861, 51
- Ingram, A.; Motta, S., 2020, *New Astronomy Reviews*, arXiv:2001.08758
- Ivezic, Z.; Connolly, A. J.; VanderPlas, J. T.; Gray, A. 2019, *Statistics, Data Mining, and Machine Learning in Astronomy: A Practical Python Guide for the Analysis of Survey Data*, ISBN: 9780691197050, Princeton University Press
- James, M; Paul, B.; Devasia, J.; Indulekha, K., 2010, *MNRAS*, 407, 285
- Jin, Chichuan; Done, Chris; Ward, M., 2021, *MNRAS*, 500, 2475
- Kelly, B. C.; Bechtold, J.; Siemiginowska, A., 2009, *ApJ*, 698, 895
- Kelly, B. C.; Becker, A. C.; Sobolewska, M.; Siemiginowska, A.; Uttley, P., 2014, *ApJ*, 788, 33
- Kochanek, C. S.; Shappee, B. J.; Stanek, K. Z.; et al., 2017, *PASP*, 129, 4502
- Kollatschny, W.; Weilbacher, P. M.; Ochmann, M. W.; Chelouche, D.; Monreal-Ibero, A.; Bacon, R.; Contini, T., 2020, *A&A*, 633, 79
- Komossa, S., Burwitz, V., Hasinger, G., Predehl, P., Kaastra, J. S., Ikebe, Y., 2003, *ApJL*, 582, L15
- Komossa, S., Zhou, H., Lu, H. 2008, *ApJ*, 678, L81
- Kormendy, J.; Fisher, D. B.; Cornell, M. E.; Bender, R., 2009, *ApJS*, 182, 216
- Kovacevic, A. B., Popovic, L. C., Simic, S., Ilic, D., 2019, *ApJ*, 871, 32
- Kovacevic, A. B.; Yi, T.; Dai, X.; et al., 2020, *MNRAS*, 494, 4069
- Kozlowski, S., et al., 2010, *ApJ*, 708, 927
- Kushwaha, P.; Sarkar, A.; Gupta, Alok C.; Tripathi, A.; Wiita, P. J., 2020, *MNRAS*, 499, 653
- Li, X.; Cai, Y.; Yang, H.; Luo, Y.; Yan, Y.; He, J.; Wang, L., 2021, *MNRAS*, 506, 2540
- Liao, Wei-Ting; Chen, Yu-Ching; Liu, X.; et al., 2021, *MNRAS*, 500, 4025
- Lin, D. C.; Irwin, J. A.; Godet, O.; Webb, N. A.; Barret, D., 2013, *ApJL*, 776



- Liu, J., Eracleous, M., Halpern, J. P., 2016, *ApJ*, 817, 42
- Liu, T., Gezari, S., Heinis, S., et al., 2015, *ApJL*, 803, L16
- Liu, T., Gezari, S., Miller M. C., 2018, *ApJL*, 859, L12
- Lomb, N. R. 1976, *Ap&SS*, 39, 447
- MacLeod, C. L., Ivezić, Z., Kochanek, C. S., et al., 2010, *ApJ*, 721, 1014
- Madejski, G.; Sikora, M., 2016, *ARA&A*, 54, 725
- Markowitz, A.; Reeves, J. N.; Braito, V., 2006, *ApJ*, 646, 783
- Mayer, L., Kazantzidis, S., Escala, A., Callegari, S., 2010, *Natur*, 466, 1082
- Mayer, L., 2013, *Classical and Quantum Gravity*, 30 244008
- Mayer, L., Bonoli, S., 2019, *Reports on Progress in Physics*, 82, 016901
- McHardy, I. M.; Koerding, E.; Knigge, C.; Uttley, P.; Fender, R. P., 2006, *Nature*, 444, 7
- Merritt, D., 2006, *ApJ*, 648, 976
- Morgan, C. W.; Kochanek, C. S.; Morgan, N. D.; Falco, E. E., 2010, *ApJ*, 712, 1129
- Nardini, E., 2017, *MNRAS*, 471, 3483
- Obric, M.; Ivezić, Z.; Best, P. N., et al., 2006, *MNRAS*, 370, 1677
- Otero-Santos, J.; Acosta-Pulido, J. A.; Becerra Gonzalez, J.; et al., 2020, *MNRAS*, 492, 5524
- Papadakis, I. E.; Lawrence, A., 1993, *Natur*, 361, 233
- Paris, I.; Petitjean, P.; Aubourg, E.; et al., 2018, *A&A*, 613, 51
- Pasham, D. R.; Strohmayer, T. E.; Mushotzky, R. F.; 2014, *Nature*, 513, 74
- Peterson B. M., et al., 2004, *ApJ*, 613, 682
- Piconcelli, E., Vignali, C., Bianchi, S., et al., 2010, *ApJL* 722, L147
- Popovic, L. C., 2012, *NewAR*, 56, 74
- Reardon, D. J., Hobbs, G., Coles, W., et al., 2016, *MNRAS*, 455, 1751
- Reines, A. E.; Reynolds, M. T.; Miller, J. M.; et al., 2016, *ApJL*, 830, L35
- Remillard, R. A.; McClintock, J. E., 2006, *ARA&A*, 44, 49
- Rees, M. J., 1984, *ARA&A*, 22, 471
- Rodriguez, C., Taylor, G. B., Zavala, R. T., Pihlstrom, Y. M., Peck, A. B., 2009, *ApJ*, 697, 37
- Sandrinelli, A.; Covino, S.; Treves, A.; et al., 2018, *A&A*, 615, 118
- Scargle, J. D. 1982, *ApJ*, 263, 835
- Sesana, A.; Haiman, Z.; Kocsis, B.; Kelley, L. Z., 2018, *ApJ*, 856, 42
- Serafinelli, R.; Severgnini, P.; Braito, V., et al., 2020, *ApJ*, 902, 10
- Shappee, B. J.; Prieto, J. L.; Grupe, D.; et al., 2014, *ApJ*, 788, 48
- Shen, Y.; Loeb, A., 2010, *ApJ*, 725, 249
- Shen, Y.; Richards, G. T.; Strauss, M. A; et al., 2011, *ApJS*, 194, 45
- Silk, J. & Rees, M. J. 1998, *A&A*, 331, L1
- Smith, K. L., Shields, G. A., Bonning, E. W., McMullen, C. C., Salviander, S. 2009, *ApJ*, 716, 866
- Smith, K. L.; Mushotzky, R. F.; Boyd, P. T.; Wagoner, R. V., 2018, *ApJL*, 860, L10
- Songsheng, Y.; Xiao, M.; Wang, J.; Ho, L. C., 2020, *ApJS*, 247, 3
- Starkey, D. A.; Horne, K.; Villforth, C., 2016, *MNRAS*, 456, 1960
- Storchi-Bergmann, T.; Nemmen da Silva, R., Eracleous, M., et al., 2003, *ApJ*, 598, 956
- Ulrich, M. H.; Maraschi, L.; Urry, C. M., 1997, *ARA&A*, 35, 445
- van den Eijnden, J.; Ingram, A.; Uttley, P.; et al., 2017, *MNRAS*, 464, 2643
- van der Klis, M., 2000, *ARA&A*, 38, 717
- van der Klis, M., 1989, *ARA&A*, 27, 517
- VanderPlas, J. T., 2018, *ApJS*, 236, 16
- Vaughan, S.; Uttley, P.; Markowitz, A. G.; et al., 2016, *MNRAS*, 461, 3145
- Verbiest, J. P. W., Lentati, L., Hobbs, B., et al., 2016, *MNRAS*, 458, 1267
- Vestergaard, M., Peterson, B. M. 2006, *ApJ*, 641, 689
- Wagoner, R. V., 2012, *ApJL*, 752, L18
- Wang, L., Greene, J. E., Ju, W., Rafikov, R. R., Ruan J. J., Schneider, D. P., 2017, *ApJ*, 834, 129
- Zechmeister, M.; Kurster, M., 2009, *A&A*, 496, 577
- Zhang, X. G., Feng L. L., 2017, *MNRAS*, 464, 2203
- Zhang, X. G., 2021a, *MNRAS*, 502, 1158, arXiv2012.15417
- Zhang, X. G., 2021b, *ApJ*, 909, 16, arXiv2101.02465
- Zhang, X. G., 2021c, *ApJ* accepted, arXiv2107.09214
- Zheng, Zhen-Ya; Butler, Nathaniel R.; Shen, Y.; et al., 2016, *ApJ*, 827, 56
- Zhou, H., Wang, T., Zhang, X., Dong, X., Li, C. 2004, *ApJL*, 604, L33
- Zu, Y.; Kochanek, C. S.; Kozłowski, S.; Udalski, A., 2013, *ApJ*, 765, 106
- Zu, Y.; Kochanek, C. S.; Kozłowski, S.; Peterson, B. M., 2016, *ApJ*, 819, 122